Nuclear Science and Techniques (2023) 34:92
https://doi.org/10.1007/s41365-023-01235-x

Design of 50 MeV proton microbeam based on cyclotron accelerator

Hong-Jin Mou[1,2,3] · Guang-Bo Mao[1,2,3] · Jin-Quan Zhang[1] · Can Zhao[1] · Jin-Long Guo[1,3] · Wen-Jing Liu[1] · Ru-Qun Wu[1] · Cheng Shen[1] · Lei Zhang[1,3] · Jun-Shuai Li[2] · Guang-Hua Du[1,3]

Received: 19 November 2022 / Revised: 24 March 2023 / Accepted: 2 April 2023 / Published online: 24 June 2023

Abstract
High-energy proton microbeam facilities are powerful tools in space science, biology and cancer therapy studies. The primary limitations of the 50 MeV proton microbeam system are the poor beam quality provided by the cyclotron and the problem of intense scattering in the slit position. Here, we present an optical design for a cyclotron-based 50 MeV high-energy proton microbeam system with a micron-sized resolution. The microbeam system, which has an Oxford triplet lens configuration, has relatively small spherical aberrations and is insensitive to changes in the beam divergence angle and momentum spread. In addition, the energy filtration included in the system can reduce the beam momentum spread from 1 to 0.02%. The effects of lens parasitic aberrations and the lens fringe field on the beam spot resolution are also discussed. In addition, owing to the severe scattering of 50 MeV protons in slit materials, a slit system model based on the Geant4 toolkit enables the quantitative analysis of scattered protons and secondary particles. For the slit system settings under a 10-micron final beam spot, very few scattered protons can enter the quadrupole lens system and affect the focusing performance of the microbeam system, but the secondary radiation of neutrons and gamma rays generated at the collimation system should be considered for the 50 MeV proton microbeam. These data demonstrate that a 50 MeV proton microbeam system with a micron-sized beam spot based on a cyclotron is feasible.

Keywords 50 MeV proton · Microbeam · Beam optics · Aberrations · Scattering

1 Introduction

Astronauts and spacecraft are irradiated by high-energy particles from galactic cosmic radiation (GCR) and solar particles (SPs) during the exploration of the Moon, Mars and other asteroids, which could cause health damage to astronauts and increase the risk of spacecraft failure [1]. The lack of knowledge regarding the biological effects caused by space radiation and countermeasures for them is currently an important factor limiting the assessment of radiation risks in human space exploration [2]. Approximately 87% of GCR energetic particles outside the solar system are protons. The energy of these protons is sufficient to penetrate several centimeters of biological tissues and organic and inorganic materials, which means that, on average, a proton passes through every cell nucleus in an astronaut's body every few days during transit outside of low earth orbit (LEO) [3, 4]. In addition, SPs, which are unpredictable and intermittent, produce a high-density flux of protons with energies greater than 30 MeV, posing a challenge for spacecraft shielding and astronaut health protection [5]. Therefore, it is essential to conduct risk assessments of high-energy proton-induced irradiation effects in space environments for long-term manned space missions. The large range of 50 MeV protons in materials makes them ideal tools for irradiating living samples in air to simulate low-dose high-energy proton environments in space. Consequently, a 50 MeV proton microbeam facility that can provide accurate irradiation at a

This work was supported by the National Natural Science Foundation of China (Nos. 1197283 and U1632271) and the National Key R&D Program of China (No. 2021YFA1601400).

✉ Guang-Hua Du
gh_du@impcas.ac.cn

[1] Material Research Center, Institute of Modern Physics, Chinese Academy of Sciences, Lanzhou 730000, China

[2] School of Materials and Energy, Lanzhou University, Lanzhou 730000, China

[3] University of Chinese Academy of Sciences, Beijing 100049, China

low dose level is an ideal platform for simulating the space radiation environment.

Proton microbeam facilities have been constantly developing since the first focused proton microbeam facility was built in the UK in 1968 [6]. To date, proton microbeam facilities have two main developmental directions: reducing the beam spot size and increasing the beam energy. A proton microbeam system with higher resolution can be used primarily for proton beam writing [7, 8] and material analysis, and can also be combined with targeted irradiation to achieve fixed-point quantitative irradiation of biological cells or animals [9–14]. With the help of a high-brightness ion source and an excellent accelerator, a beam spot size of 20 nm has been achieved at the second-generation proton writing microbeam facility at the National University of Singapore [15]. In addition, higher-energy proton microbeam facilities are needed in studies on the simulation of space irradiation effects and the evaluation of the radiation resistance of space devices, as well as studies on proton therapy that require quantitative targeted irradiation of cancer cells and organs [16–20].

In the coming decades, there will be demanding multiscale biomedical studies on low-dose high-energy proton radiation concerning risk assessment and radiation protection for planned projects of manned lunar base and Mars exploration. However, most proton microbeam facilities currently in operation have energies between 1 and 6 MeV [21]. In contrast, the world's highest energy proton microbeam system, which is based on the Munich tandem accelerator at SNAKE, Germany, has a maximum energy of 30 MeV [22]. Proton microbeam systems based on a tandem or electrostatic accelerator with higher energy have not been reported, which is explained by the following difficulties. First, as accelerator technology and the cost limit the development of higher-energy (> 30 MeV) tandem accelerators, high-energy protons with energies higher than 30 MeV are usually provided by cyclotrons. For example, a 40 MeV proton microbeam system based on a cyclotron with a 10-μm beam diameter has been reported at the University of Manitoba Accelerator Laboratory [23]. Electrostatic accelerators cannot afford proton beams of such high energy, whereas linear accelerators with high current have disadvantages in terms of high beam intensity on the microslit and a high yield of secondary radiation. Compared with the electrostatic accelerators and tandem accelerators commonly used in proton microbeam systems, cyclotrons provide poor beam quality; Furthermore, the beam emittance and momentum spread of cyclotrons, owing to the high-frequency waveform acceleration, are much larger (by approximately two orders of magnitude) than those of electrostatically accelerated beams. Second, higher-energy protons, such as those at 50 MeV, have a range of millimeters in common slit materials such as tungsten carbide and even centimeters in water, whereas protons with energies of 3 MeV only have ranges of tens of microns in these materials. The transparent zone induced by beam scattering at the microslit edge for higher-energy protons is much larger than the object slit opening. A large number of scattered particles with large divergence angles and momentum spread are not favorable for focusing the microslit-collimated beam onto a micron-sized beam spot.

Therefore, because of the above difficulties of a high-energy microbeam system based on a cyclotron, it is necessary to effectively eliminate the scattered particles generated in the slit system and to rationally select the focusing lens configuration. In the PTB microbeam facility, a 90° bending magnet was placed behind the beam defining slits to separate the unscattered and scattered particles [10]. In the IMP-Lanzhou microbeam facility, based on a cyclotron complex, a symmetrically achromatic system composed of two identical 45° bending magnets and a quadrupole magnet in between, and a slit situated before the second 45° bending magnet that can be used for energy analysis, was used to deflect the ion beam downward to a quadrupole–triplet focusing system [24, 25]. The deflected beamline structure provided a pure ion beam, which was delivered to the experimental terminal in a limited space. In the SNAKE microbeam system, a 30-m-long beamline (from the object slits to the focusing lens) was used to minimize the effects of slit scattering and secondary radiation at the terminal [26]. In the QST-Takasaki microbeam system based on an AVF cyclotron, the Russian quadruplet configuration with small chromatic aberrations was chosen, and a flattop acceleration technique was introduced to minimize the beam energy spread [27].

To provide a radiation platform for ground-based studies related to the Chinese manned lunar project, a high-energy microbeam system based on a 50 MeV proton cyclotron is proposed. In this work, we first studied the beam optics of a microbeam facility with an Oxford triplet lens system and analyzed the stability of this system to changes in the divergence angle and momentum spread. We then simulated the beam momentum spread filtering ability of the energy collimator in this microbeam system and analyzed the effects of quadrupole lens parasitic aberrations and lens fringe field. Finally, a slit system model was established using the Geant4 toolkit, and the scattering of protons at the slit in this system was evaluated.

2 Design of the 50 MeV proton microbeam system

Radiation effect studies in space science and biology require living biological samples to be irradiated in the atmosphere with a precise number of protons targeting a micron-sized area, and a vertical beam line is preferred for irradiating samples kept in a liquid medium. However, only cyclotrons

or linear accelerators are capable of producing high-energy protons with energies above 50 MeV, whose energy spread is one to three orders of magnitude worse than that of electrostatic accelerators owing to their technical design. The magnetic rigidity of the 50 MeV proton is 1.06 T•m, which is about four times higher than that of most proton microbeams. To achieve the radiation parameters required to explore the scientific questions in space radiation research, we introduced a high-energy proton microbeam system based on the proton cyclotron built by the China Institute of Atomic Energy, which can deliver protons ranging from 30 to 50 MeV.

A schematic of the 50 MeV proton microbeam system is shown in Fig. 1. The main beam is transported through the achromatic beam optics and waist–waist transfer from the front beamline and forms a beam waist in both directions at the entrance collimator of the microbeam beamline. The microbeam system consists of three main parts. First, a 90-degree bending magnet is used to deflect the beam direction from horizontal to vertically upward, which is beneficial for irradiating biological samples, and its edge angle can provide weak focusing in the horizontal direction of the beam, thus increasing the beam transport efficiency at the object microslit. The second part is a slit system composed of an object slit and a divergence defining slit, which defines the acceptance of the microbeam system and allows very few protons to enter the focusing magnets. The third part is an Oxford triplet lens system, which is widely used in many microbeam facilities and can focus the ion beam to form a microscale probe on the target; this is the core of the microbeam system [28]. In addition, the beam envelope of the Oxford triplet lens system for a 50 MeV proton microbeam system, simulated using WinTRAX, is shown in Fig. 2. It represents the trajectory of particles in the direction of beam transmission in the 50 MeV proton microbeam line. The transfer efficiency of the microbeam line is 2.5×10^{-6} in the 10-μm slit settings.

According to the construction of the 50 MeV proton cyclotron laboratory, the free space for the establishment of the proton microbeam is approximately 7 m high in the vertical direction. Based on the beam quality of the cyclotron accelerator, the Oxford triplet lens system, which has low aberration coefficients, is preferred for focusing ion beams with large divergence angles and energy spreads. As shown in Fig. 1, the 90° bending magnet has a bending radius of 0.74 m and an edge angle of 27°; each quadrupole lens of the focusing triplet lens system is designed with an effective length of 10 cm, a bore diameter of 15 mm and a maximum pole-tip field of 0.9 T. Furthermore, the distance between the centers of adjacent lenses is 20 cm, which can provide sufficient focusing force for the 50 MeV proton beam. The collimator–dipole magnet–object system functions as an energy refiner that can define a beam with a given energy and restrict the energy spread by the collimator/slit opening. In addition, after the beam energy is filtered at the object slit position, the beam intensity is reduced by four to five orders of magnitude, so that the beam current after the object slit is only on the order of fA; therefore, we only need to consider the radiation protection shield at the object slit position.

3 Beam optics of 50 MeV proton microbeam system

3.1 Beam optics and ray tracing

The ion beam optical parameters of this microbeam system were calculated using WinTRAX [29], Zgoubi [30, 31]

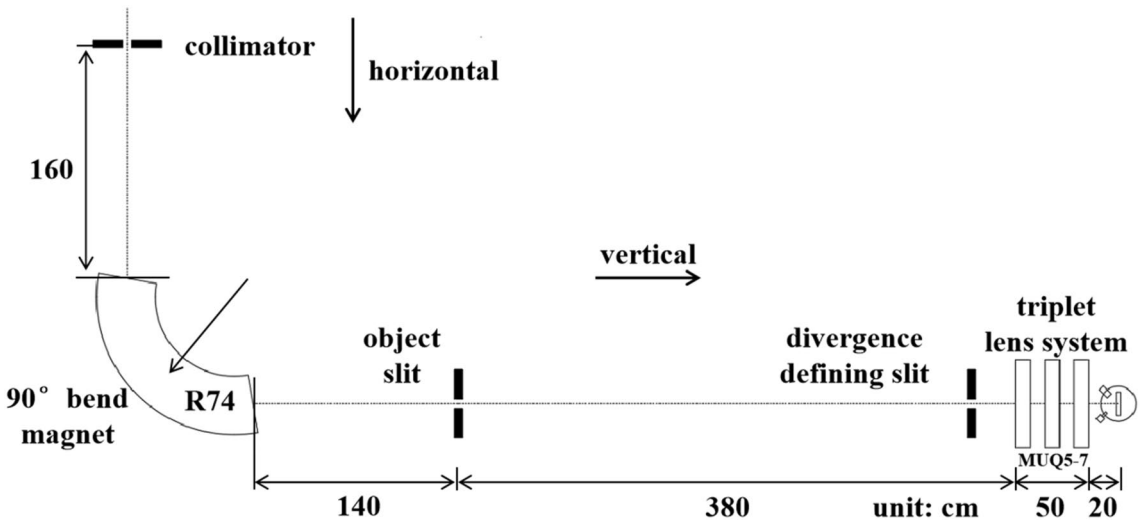

Fig. 1 Scheme of the 50 MeV proton microbeam system

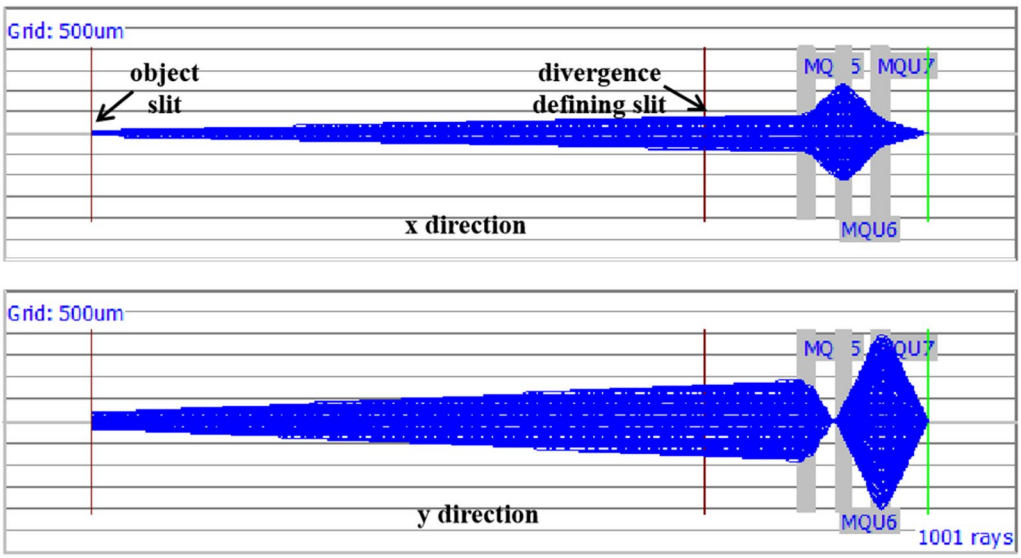

Fig. 2 (Color online) Beam envelope of the 50 MeV proton microbeam system

and PRAM [32]. These software packages are commonly used in the microbeam community. Protons with energies of 50 MeV are used as examples in the following calculations. Without additional explanation, all subsequent simulations and analyses began with the beam at the object slit in the microbeam system. Table 1 lists the beam optical parameters of the microbeam system with the Oxford triplet lens configuration. At the object slit, we take a set of Cartesian coordinates; the positive z-axis coincides with the direction of the beam motion, the x-axis is defined as horizontal, and the y-axis is defined as vertical. When the lens was perfectly aligned, the lens axes coincided with the z-axis, and the antisymmetric planes coincided with the xz and yz planes.

We then studied the aberration in this probe-forming system to examine the robustness and tolerance according to the beam parameters and related factors. In most microbeam systems, the ion beam is focused using a combination of magnetic quadrupole lenses. A quadrupole lens is described as converging, "C," if a particle moving in the xz plane is deflected toward the axis, and diverging, "D,"

Table 1 Beam optical parameters for triplet lens configuration were calculated by WinTRAX

Factor	Oxford triplet
Demagnification factor	
D_x	−11.12
D_y	36.15
Chromatic aberration coefficients (μm/mrad%)	
$<x/\theta\delta>$	460.87
$<y/\varphi\delta>$	−184.77
Spherical aberration coefficients (μm/mrad^3)	
$<x/\theta^3>$	−28.74
$<x/\theta\varphi^2>$	−25.5
$<y/\varphi^3>$	10.56
$<y/\theta^2\varphi>$	7.87
α (rad^2/m^2)	0.47
Q (mrad^2/μm$^{2/3}$)	64
Excitation of the 1st and 2nd lenses (T)	0.627
Excitation of the 3rd lens (T)	0.747
Slit parameters with 10-μm final beam diameter (μm^2 mrad^2)	110×0.2×360×0.4=3168
Slit parameters with 1-μm final beam diameter (μm^2 mrad^2)	10×0.04×36×0.04=0.576
Momentum spread (%)	0.02

if the particle is deflected away from the axis. Considering the beamline arrangement and microbeam adjustability, the triplet configuration was designed with a $D_1C_1D_2$ structure. Having the same numerical subscript indicates that the two magnetic lenses are coupled to the same power supply. For a focusing microbeam system, the position change of an ion from the object plane to the image plane can be expressed by Eq. (1) [32]:

$$\begin{aligned} x_i &= \langle x/x\rangle x_0 + \langle x/\theta\rangle\theta_0 + \langle x/\theta\delta\rangle\theta_0\delta_0 + \left\langle x/\theta^3\right\rangle\theta_0^3 + \left\langle x/\theta\varphi^2\right\rangle\theta_0\varphi_0^2 + \cdots \\ y_i &= \langle y/y\rangle y_0 + \langle y/\varphi\rangle\varphi_0 + \langle y/\varphi\delta\rangle\varphi_0\delta_0 + \left\langle y/\varphi^3\right\rangle\varphi_0^3 + \left\langle y/\theta^2\varphi\right\rangle\theta_0^2\varphi_0 + \cdots, \end{aligned} \tag{1}$$

where (x_0, θ_0, y_0, φ_0) represent the position and divergence angle of the initial beam in the object plane defined by a slit system consisting of an object slit and a divergence defining slit, δ_0 is the particle momentum spread relative to the beam mean momentum, and x_i and y_i represent the ion position at the image plane. The demagnification factor of the microbeam system is defined as $D_x = <x/x>^{-1}$, $D_y = <y/y>^{-1}$, $<x/\theta>$ and $<y/\varphi>$ are the astigmatism coefficients (in a well-focused microbeam system, the astigmatism coefficients are zero), $<x/\theta\delta>$ and $<y/\varphi\delta>$ are the chromatic aberration coefficients, and $<x/\theta^3>$, $<x/\theta\varphi^2>$, $<y/\varphi^3>$ and $<y/\theta^2\varphi>$ are the spherical aberration coefficients. The factors α and Q, which represent the image sharpness of the focused beam object, are used to judge the performance of microbeam systems [33, 34].

$$\alpha = \frac{D_x \cdot D_y}{\langle x/\theta\delta\rangle \cdot \langle y/\varphi\delta\rangle} \tag{2}$$

$$Q = \frac{D_x \cdot D_y}{\left\langle x/\theta^3\right\rangle \cdot \left\langle x/\theta\varphi^2\right\rangle \cdot \left\langle y/\varphi^3\right\rangle \cdot \left\langle y/\theta^2\varphi\right\rangle} \tag{3}$$

Generally, larger values of α and Q for a microbeam system indicate superior performance. From the beam optical parameters of this system and the given beam parameters, spherical aberrations are nearly one-tenth of the chromatic aberrations for beam parameters of 10-micron and 1-micron final beam spots, indicating that the chromatic aberrations are the dominant aberrations. Therefore, the α factor is more suitable for describing the performance of this system. In addition, two sets of slit parameters and momentum spread of the microbeam system, defined as $x_0{\cdot}\theta_0{\cdot}y_0{\cdot}\varphi_0$, were calculated for beam spots with diameters of 10 μm and 1 μm on the target, respectively. As shown in Table 1, compared to most other microbeam systems, this system has relatively small demagnification factors in both directions. This is a consequence of the short object distance of the system, and the main reason is the high magnetic rigidity of 50 MeV protons limits the use of high-demagnification and high-excitation lens configuration. In addition, spherical aberrations of this system can be ignored when the initial beam divergence angles are less than 0.1 mrad, and chromatic aberrations are the main factors affecting the final beam spot size. It is worth noting that although the primary beam has a momentum spread of 1%, the dipole magnet and collimator–slit combination resulted in a momentum spread of only 0.02% within the beam entering the focusing quadrupole magnets, at the cost of intensity reduction.

The remainder of this paper analyzes the beam spot distribution in the phase space according to the characteristics of the Oxford triplet lens system, with final beam diameters of 10 μm (object slit 110 μm × 360 μm, divergence defining slit 0.2 mrad × 0.4 mrad (660 μm × 1320 μm), full width if not specified) and 1 μm (object slit 10 μm × 36 μm, divergence slit 0.04 mrad × 0.04 mrad (132 μm × 132 μm)), and a beam momentum spread of 0.02% (full width). As shown in Fig. 3, ray tracing was performed with 10,000 particles starting from the object slit with the triplet lens system using Zgoubi. Figure 3 shows the distribution of 10,000 particles in the phase space for the two different slit parameters on the target, as well as the variation in the final beam density along the x and y directions. It can be seen that these particles are evenly distributed in the phase space without significant distortion, thanks to the small aberration coefficients of this system.

3.2 Intrinsic aberrations

Intrinsic aberrations are aberrations determined by the structural design of the quadrupole lens system, mainly including chromatic and spherical aberration terms. Intrinsic aberrations induce blur and deformation of the beam spot from the ideal image of the object; they exist in the case of ideal processing of the lens and need to be minimized in the beam optical design. To examine the tolerance of the final beam size to the change of the divergence angle in both directions and momentum spread, the beam spot size with different inputs (mainly toward the larger beam spot) was calculated using Zgoubi for both the 10-micron and 1-micron solutions. The divergence angles θ_0 in the x direction and φ_0 in the y direction (from 0.05 to 0.6 mrad, FWHM) were adjusted by the divergence defining slit opening while the object slit remained, and the momentum spread δ_0 varied from 0.01 to 0.1% (FWHM). Figure 4 shows the beam spot size change at the image plane as a function of the divergence angle θ_0, φ_0 and momentum spread δ_0 for our triplet lens system. The data points marked with stars in the figure represent the calculations using the designed input given in Table 1. In each

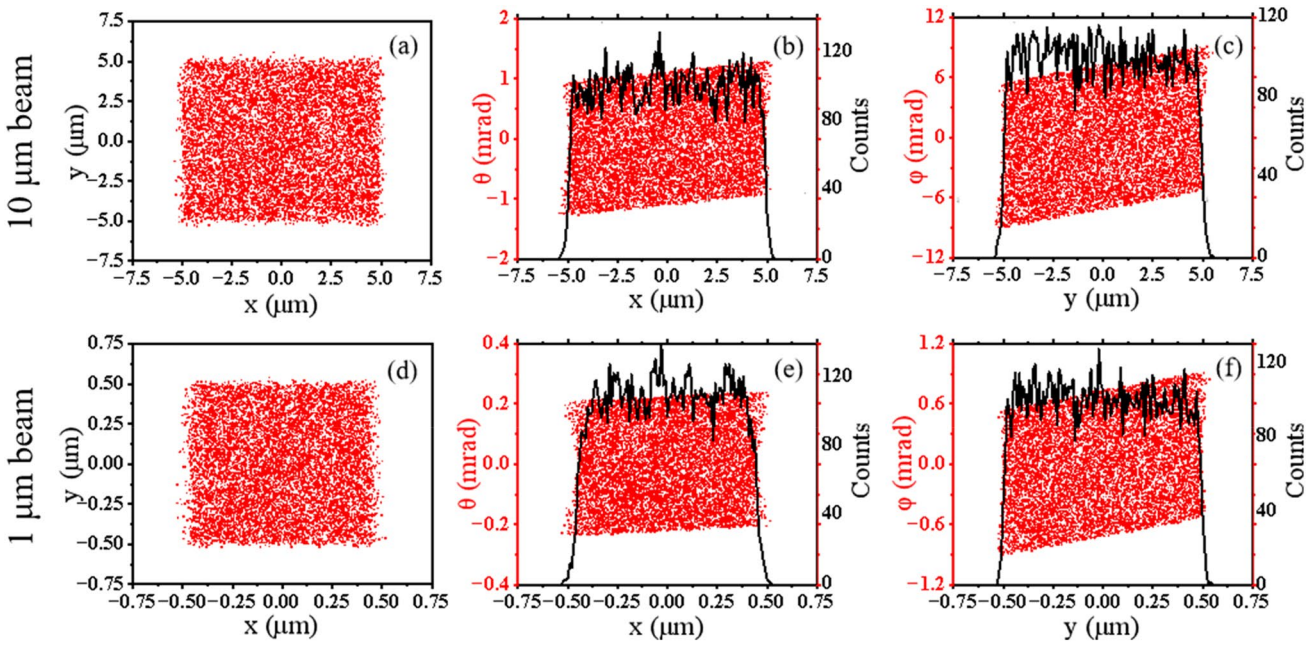

Fig. 3 (Color online) Spatial and phase-space distributions of protons and proton density change in the x and y directions at the focused image plane, ray-traced with 10,000 protons. The beam spots at the image plane are 10 μm × 10 μm (**a**–**c**) and 1 μm × 1 μm (**d**–**f**). Parameters are given in Table 1

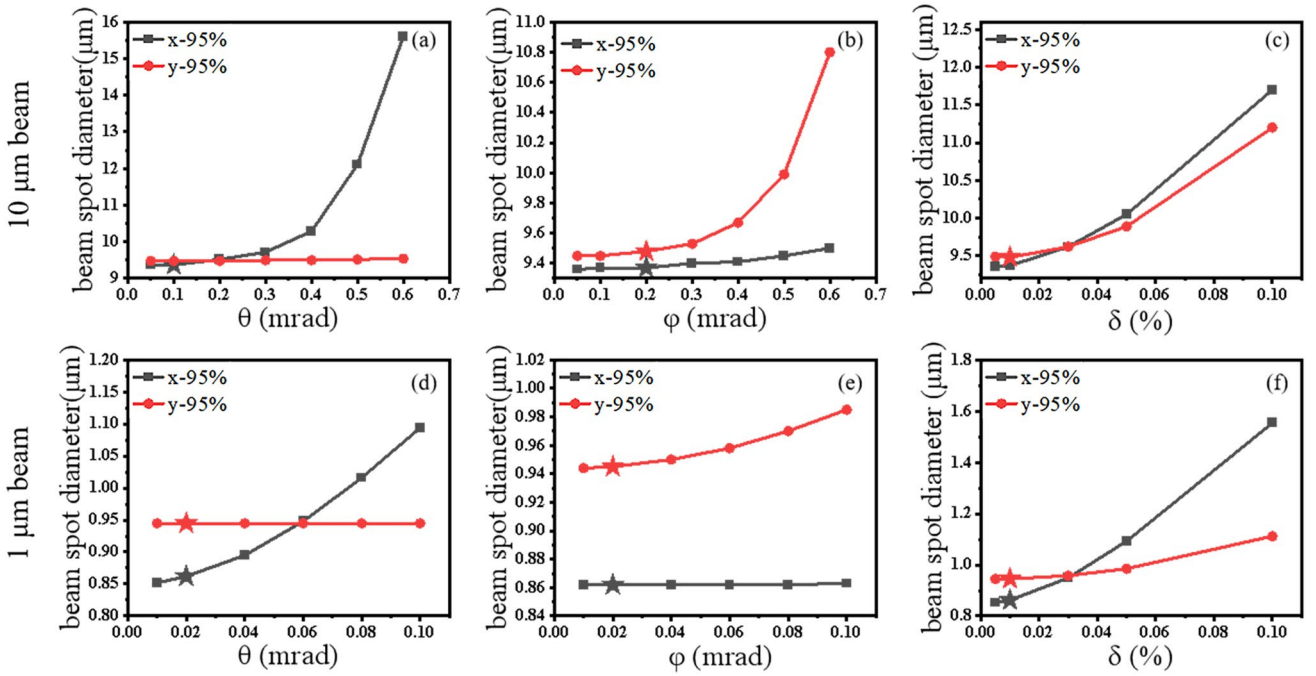

Fig. 4 Microbeam spot size depends on divergence angle θ_0, φ_0 and momentum spread δ_0 for the triplet lens system

illustration, only the given parameter was varied, whereas the other parameters remained at the designed values.

The spherical and chromatic aberrations depend on the beam divergence angle and momentum spread, which can be defined by the slit and bending system. With the given slit setting and the beam parameters (θ_0 and φ_0 at the level of 0.2 mrad and δ_0 of about 0.02%), the data in Fig. 4 demonstrate that the beam spot size is mainly influenced by the

chromatic aberrations. The chromatic and spherical aberration coefficients in the x direction for the Oxford triplet lens system are larger than those in the y direction, so they are more sensitive to changes in the divergence angle and momentum spread in the x direction.

The low aberration coefficients of the Oxford triplet lens system results in a relatively small increase in the final beam spot size relative to the increase in the divergence angle. For example, in the 10-micron solution, the increase in the divergence angle θ_0 from 0.1 to 0.4 mrad results in an increase of 0.92 μm for the final beam spot size (Fig. 4a), whereas the increase in φ_0 from 0.1 to 0.4 mrad results in an increase of 0.22 μm (Fig. 4b), and the increase in the momentum spread δ_0 from 0.01 to 0.05% results in an increase of 0.68 μm (Fig. 4c). For the 1-micron solution, the increase in the divergence angle θ_0 from 0.02 to 0.1 mrad results in an increase of 0.23 μm for the final beam spot size (Fig. 4d), the increase in φ_0 from 0.02 to 0.1 mrad results in an increase of 0.04 μm (Fig. 4e), and the increase in the momentum spread δ_0 from 0.01 to 0.05% results in an increase of 0.23 μm (Fig. 4f). These plots demonstrate that this system is not sensitive to changes in the divergence angle and momentum spread within a particular range, indicating that our triplet lens systems with low aberration coefficients are suitable for focusing an ion beam with a large divergence angle and momentum spread.

3.3 Energy filtration

The combination of a bending magnet and a slit can filter the momentum spread of the particles [35]. Considering the large energy spread of the 50 MeV cyclotron proton beam, a 90-degree bending magnet together with a slit system was included in this microbeam system, and the energy collimation function was simulated using Zgoubi. It is assumed that the initial beam parameters before the 90-degree bending magnet were $x = y = 0.1$ mm, $\theta = \varphi = 1$ mrad and $\delta_0 = 1\%$ (full width), and 400,000 protons were traced in the Oxford triplet lens system with initial beam parameters for the 10-μm beam spot. As shown in Fig. 5, only approximately 136 protons reached the target. It can be seen that the sizes of these protons in both the x and y directions are within 10 microns, and the plot of the momentum of these protons shows that the momentum spread of the focused protons is within 0.015%, which demonstrates the momentum filtering ability of the energy collimator. However, considering the high penetration depth of the 50 MeV protons in the slit material, the actual effect of the energy collimator requires further study, so $\delta_0 = 0.02\%$ is chosen as a conservative estimate here.

3.4 Parasitic aberrations

Parasitic aberrations are mainly caused by the misalignment of the lens and can be reduced by fine installation and collimation of the lens. Parasitic aberrations include rotational, displacement and power ripple (magnetic excitation) aberrations. Figure 6 shows the geometrical aberrations applied to a quadrupole lens with the number n [32]. The main parasitic aberration coefficients of each quadrupole lens in the microbeam system are listed in Table 2, in which the index represents the number of quadrupole lenses, U represents lens translation (μm) along the x-axis, V represents lens translation (μm) along the y-axis, ρ represents lens rotation (mrad) around the beam axis and ε represents the power supply ripple (%) of the lens. (Lenses 1 and 2 are coupled to a power supply.) The last column shows the lens translation and rotation and power supply ripple precision required to keep the corresponding displacement of the beam spot on the target to less than 1 μm. The calculated results of PRAM and WinTRAX were very consistent and comparable to those of previous microbeam systems [36]. As some of the parasitic aberration coefficients are related

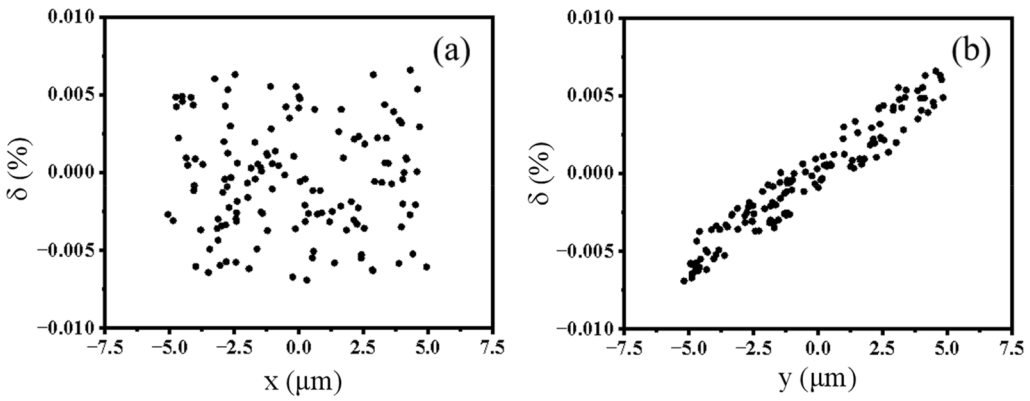

Fig. 5 Ray tracing of 400,000 particles starting before the 90-degree bending magnet. Object slit size (full width): 110 μm × 360 μm; divergence defining slit (full width): 0.2 mrad × 0.4 mrad (660 μm × 1320 μm)

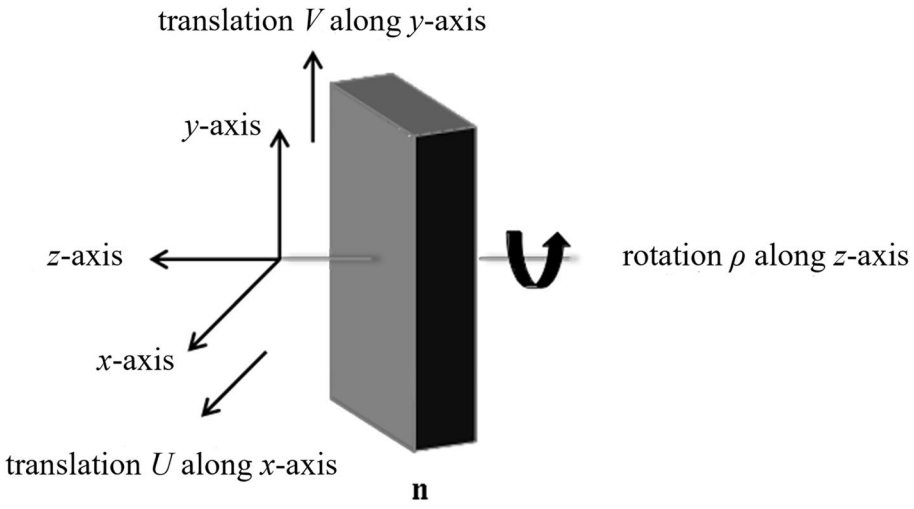

Fig. 6 Description of the misalignment parameters applied to quadrupole number *n* in the calculation of the parasitic coefficients

Table 2 List of dominant parasitic aberration coefficients calculated using PRAM and WinTRAX

Parasitic aberrations		PRAM	WinTRAX	Precise
Translation aberrations	$<x/U_1>$	3.145	3.178	0.315 μm
	$<x/U_2>$	− 7.069	− 7.036	0.142 μm
	$<x/U_3>$	2.736	2.769	0.361 μm
	$<y/V_1>$	0.720	0.748	1.337 μm
	$<y/V_2>$	0.323	0.353	2.833 μm
	$<y/V_3>$	− 2.103	− 2.074	0.482 μm
Rotation aberrations	$<x/\varphi\rho_1>$	21.014	21.019	0.119 mrad
	$<x/\varphi\rho_2>$	22.055	22.052	0.113 mrad
	$<x/\varphi\rho_3>$	− 43.069	− 43.067	0.058 mrad
	$<y/\theta\rho_1>$	− 6.479	− 6.470	0.773 mrad
	$<y/\theta\rho_2>$	− 6.800	− 6.808	0.734 mrad
	$<y/\theta\rho_3>$	13.273	13.282	0.376 mrad
Excitation aberrations	$<x/\theta\varepsilon_1>$	− 544.72	− 542.69	0.009%
	$<x/\theta\varepsilon_2>$	93.256	93.222	0.054%
	$<y/\varphi\varepsilon_1>$	18.144	18.232	0.137%
	$<y/\varphi\varepsilon_2>$	161.82	161.92	0.015%

to the initial divergence angle of the beam, the initial divergence angles were assumed to be 0.2 mrad in the *x* direction and 0.4 mrad in the *y* direction, the same as in Table 1. The maximum quadrupole lens rotation angle and translation were less than 0.058 mrad and 0.14 μm, respectively. The maximum excitation deviation for a beam spot size increase of less than 1 μm requires the power supply ripple to be less than 0.009% (90 ppm), and such high-precision power supplies are now available on the market. The translation aberrations $<x/U>$ and $<y/V>$ have no effect on the image size and simply cause a displacement of the beam spot on the target [36]. For rotation aberrations, assuming an outer diameter of 300 mm for the lens, the rotation misalignment must be less than 8.7 μm, which is a challenge for magnet installation and correction. It can be seen that the rotation aberrations are proportion to the divergence angles θ and φ, so the effect of rotation aberrations on the beam spot can be improved by reducing the divergence angle at the expense of loss of beam current for high-resolution beam spots. In addition, the rotation aberration components of the lens can be effectively eliminated by finely adjusting the lens when the beam is online after the system is installed.

3.5 Fringe field model

The focusing properties of a quadrupole lens are determined by the distribution of its magnetic field along the longitudinal coordinate *z*. Real quadrupole lenses have fringe fields, whereas an ideal rectangular model (curve 1 in Fig. 7a) is used in the above calculations. The longitudinal fringe field profile will generally differ for each quadrupole lens. The following equation has been proposed to describe the magnetic field distribution of the lens along the longitudinal coordinate *z* [29] [37]:

$$G(z) = G_0 f(z), \tag{4}$$

where

$$f(z) = \frac{1 + e^{c_0}}{1 + e^{P(s)}}, P(s) = c_0 + c_1 s + c_2 s^2 + c_3 s^3 + \cdots, s = \frac{|z - z_0|}{r}$$

Here, *z* is the direction of the beam axis, z_0 is the length of the uniform field region, and *r* is the radius at the pole tip. G_0 is the magnetic field gradient of the lens. By changing the values of c_0 through c_5, we obtained changes in the beam optical parameters for different fringe field models. As shown in Fig. 7, the existence of different fringe fields induces an increase in the spherical aberration coefficients of the beam optical parameters. Although a slight deviation

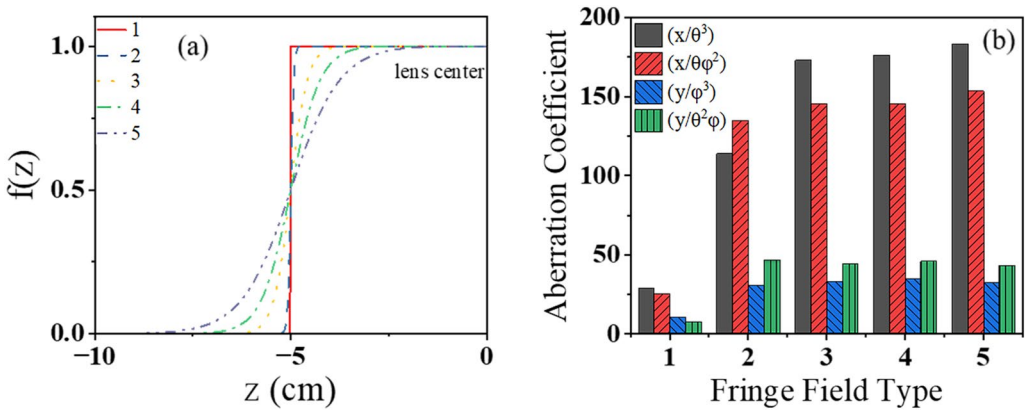

Fig. 7 (Color online) **a** Different fringe field models of quadrupole lens; **b** spherical aberration coefficients for different fringe field models with the Oxford triplet lens system. 1—Rectangular model; 2—$c_0 = -6.0$, $c_1 = 20$, $c_2 - c_5 = 0$; 3—$c_0 = -6.0$, $c_1 = 3.5$, $c_2 - c_5 = 0$; 4—$c_0 = -6.0$, $c_1 = 2.0$, $c_2 - c_5 = 0$; 5—$c_0 = -6.0$, $c_1 = 1.2$, $c_2 - c_5 = 0$

from the ideal magnet (curve 2 vs curve 1) causes dramatic effects, in which the $<x/\theta^3>$ coefficient increases from 28 to 113, further deviation does not greatly increase the spherical aberration coefficients (Fig. 7b). Despite the increase in the spherical aberrations, our further simulation showed that for different fringe field models, the final beam spot size did not change significantly. For a quadrupole lens with a length of 10 cm and a pole gap of 1.5 cm, the ratio of the length to the bore radius is much larger than 1. Therefore, its real magnetic field distribution is closer to the magnetic field distribution under the rectangular model.

4 Technical challenges

The high energy of the 50 MeV proton facilitates the irradiation of large samples with the benefit of having a long range for the target. However, this induces several challenges in the production of a clean microbeam resulting from scattering, secondary particles and radiation protection.

The main function of the slit in the microbeam system is to reduce the size of the beam object and define the beam divergence angle. This means that many secondary particles and scattered ions are produced by the collimation of the slit edge, particularly for high-energy beams. These scattered ions entering the lens system with large energy loss can affect the focusing performance of the microbeam system. Compared with the present microbeam facility with the highest ion energy (80.5 MeV/u $^{12}C^{6+}$) [38, 39], the SRIM simulation shows that the 50 MeV proton has an even longer range and worse scattering in the microslit made of WC + 8%Co (tungsten carbide, density 15.09 g/cm^3) [40]. As shown in Fig. 8, the range and lateral projective range of 50 MeV protons in WC material are 2.95 ± 0.14 mm and 0.19 ± 0.26 mm, whereas 80.5 MeV/u $^{12}C^{6+}$ ions have a range of 2.44 ± 0.05 mm and a lateral projective range of 0.04 ± 0.06 mm. These data suggest that the scattering area of 50 MeV protons in the slit material is much larger and that the slit scattering problem is more serious.

To investigate the influence of ion scattering at the slit system, the production and transportation of the scattered protons and secondary particles were studied using Geant4 simulations [41]. The slit system model was composed of a piece of solid cubic WC + 8%Co with a thickness of 3 mm; the slit consisted of four pieces of WC material with rectangular edges arranged in sequence, and the distance between the object slit and the divergence defining slit was 3.3 m. A data collection surface of 3 mm × 3 mm square was placed behind the second divergence defining slit to collect the information of particles that can pass through the slit system. The physics model in Geant4 was QGSP_BIC. Two different slit system parameters were selected for simulation: a large slit system setting with 110 μm × 0.2 mrad in the x direction and 360 μm × 0.4 mrad in the y direction (1) for a 10-μm final beam spot and a small slit system setting with 10 μm × 0.04 mrad in the x direction and 36 μm × 0.04 mrad in the y direction (2) for a 1-μm final beam spot. Finally, the momentum spread of the proton beam was 0.02% in the two slit system parameters. Using the two slit system settings, the transfer efficiency and proportion of scattered protons and secondary particles through the slit system were quantitatively analyzed.

Then, an incident beam of 10^6 protons with a diameter of 1 mm and a divergence angle of 1 mrad in both directions was shot into the slit system, as shown in Fig. 9a. With the detector behind the divergence slit, the intact proton beams, scattered protons and secondary particles were collected at different incident proton energies, as shown in Fig. 9b. The Geant4 simulations showed that the number of secondary particles and scattered protons increased with the proton

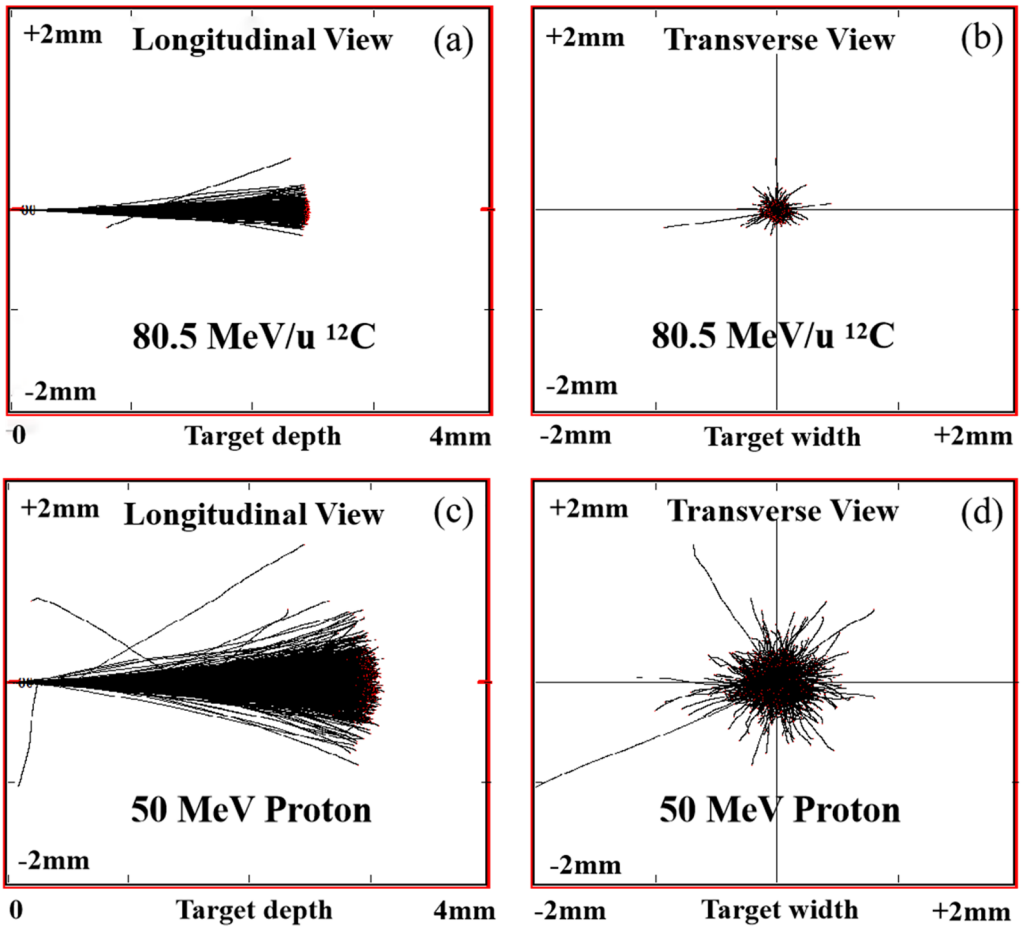

Fig. 8 Trajectories of 80.5 MeV/u $^{12}C^{6+}$ and 50 MeV proton in tungsten carbide were simulated by SRIM

energy, whereas the number of unscattered protons remained nearly unchanged. For example, when the incident proton energy was 3 MeV, the yield of scattered protons and secondary particles was less than 10^{-6}, and their proportion increased as the incident proton energy increased. When the incident proton energy reached 50 MeV, the proportion of scattered protons and secondary particles collected exceeded 10%. This means that the higher the energy of the protons, the more scattered the protons produced at the slit location. As shown in Fig. 9c, with the slit setting for the 10-μm microbeam spot given in Table 1, the proportion of scattered protons reached 12.3% for the 50 MeV protons and increased to 47.3% with the slit setting for the 1-μm microbeam spot. These data show that the effect of scattered protons is less significant for the slit setting of the 10-μm microbeam spot, whereas the percentage of scattered protons is too high for the 1-μm slit setting, which will affect the focusing performance of the quadrupole lens group.

The energy information of the passed protons was then analyzed, as shown in Fig. 9d. The energies of most of the scattered protons were much lower than 50 MeV. This indicates that most of the scattered protons underwent multiple scattering in the slit system; therefore, most of them would have a large divergence angle and be blocked by the subsequent beamline tube. To verify the above hypothesis, the data collection surface was placed at the entrance of the quadrupole lens group, as shown in Fig. 1, which was 0.5 m behind the divergence slit. The yield of scattered protons and secondary particles was drastically reduced, as shown in Fig. 9e. For the 10-μm slit setting, only 0.7% of the scattered protons were collected, and for the 1-μm slit setting, the proportion was approximately 12.6%. In addition, according to the SRIM simulation, the maximum scattering angle of the 50 MeV protons collected after passing through the 3-mm-thick tungsten carbide slit was approximately 3.23 mrad. The inner diameter of the beam tube between the two slits was designed to be 60 mm, which was much larger than the opening size of the divergence defining slit. The minimum angle required for a scattered proton produced in the object slit to be able to interact with the beam tube was approximately 9 mrad, which means that the majority of the scattered

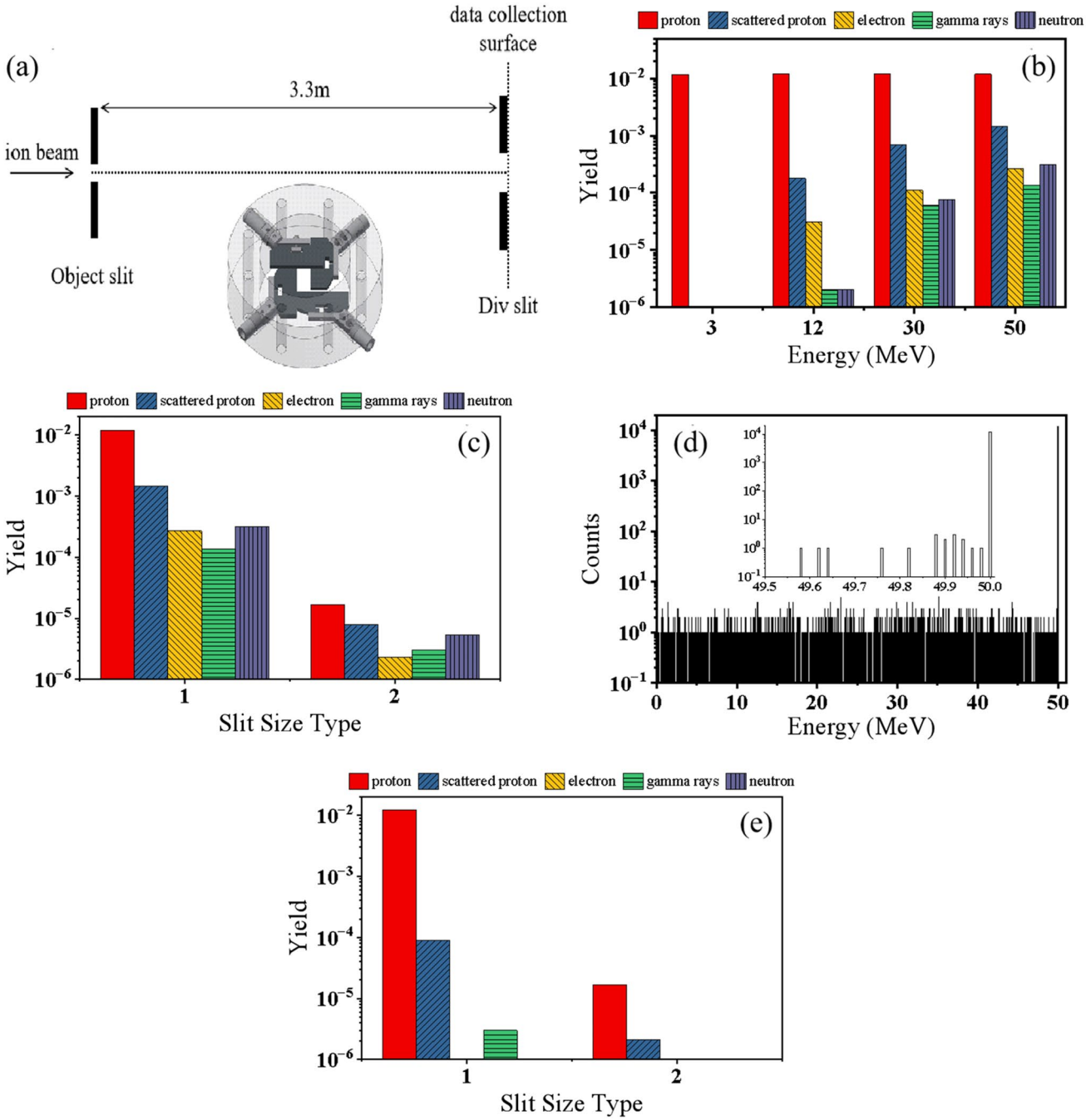

Fig. 9 (Color online) **a** Slit model in the microbeam system; **b** detected particles at different incident proton energies, where the slit system setting is 110 μm×0.2 mrad in the *x* direction and 360 μm×0.4 mrad in the *y* direction; **c** detected particles with two slit system settings of 110 μm×0.2 mrad in the *x* direction and 360 μm×0.4 mrad in the *y* direction (1) and 10 μm×0.04 mrad in the *x* direction and 36 μm×0.04 mrad in the *y* direction (2); **d** energy spectrum of the transmitted protons with the slit setting of 110 μm×0.2 mrad in the *x* direction and 360 μm×0.4 mrad in the *y* direction, where the incident proton energy is 50 MeV; **e** detected particles with two slit system settings, where the data collection surface is 0.5 m behind the divergence slit

protons could not interact with the beam tube. Moreover, the beam current before the object slit was on the order of nanoamperes; therefore, the beam tube could only contribute countable secondary particles that could enter the lens group. Consequently, very few scattered protons and secondary particles could actually enter the quadrupole lens group.

In a typical microbeam system, the main beam from the accelerator is collimated and lost in the slit system. The Geant4 calculation in Fig. 9b indicates that for most

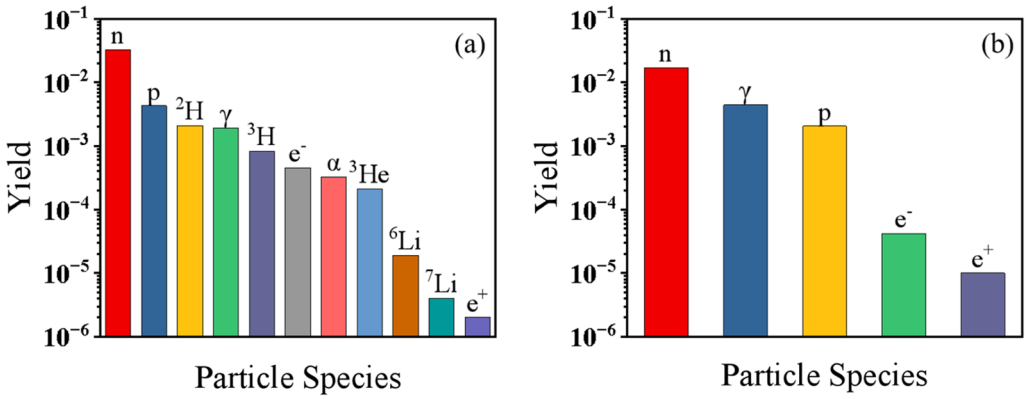

Fig. 10 (Color online) Type and yield of primary secondary particles. **a** 80.5 MeV/u $^{12}C^{6+}$; **b** 50 MeV proton

microbeams with proton energies below 3 MeV, there are no detectable radiation particles such as neutrons, gamma rays and electrons. To investigate the radiation protection of 50 MeV protons at the slit location, a target model was built using the Geant4 toolkit. In this model, 10^6 ions were used as the incident ion beam, with two different ions: 50 MeV protons and 80.5 MeV/u $^{12}C^{6+}$. The initial beam diameter was the same as in the previous simulation in Fig. 9. The target material was a piece of WC + 8%Co with a thickness of 3 mm. In contrast to the many types of secondary particles collected for 80.5 MeV/u $^{12}C^{6+}$, only five types of secondary particles were obtained on the data collection surface for the 50 MeV protons, as shown in Fig. 10. The yields of gamma rays and neutrons were relatively high at approximately 10^{-2}. However, with the energy filtration system combined with the bending magnet, most of the secondary radiation produced at the main beam loss point (the collimator at the horizontal beamline) could not reach the Oxford triplet lens system, keeping the microbeam target surroundings radiation-clean and user-friendly.

High energy is particularly advantageous for the 50 MeV proton microbeam system, but serious scattering at the slit position and poor beam quality of the 50 MeV proton beam must be considered. The Oxford triplet lens configuration with low aberrations for large beam divergence acceptance is suitable for cyclotron microbeams. Compared with previous bending microbeam systems, this microbeam has few tunable magnets (mainly the 90° bending magnet and the coupled triplet) that need to be adjusted to obtain a micron-sized beam spot; thus, it is easy to manipulate and user-friendly for trained radiobiologists. According to the simulations, the transfer efficiency of the microbeam system in the 10-μm slit settings is 2.5×10^{-6}; to achieve more than 30,000 protons per second in the 10-μm final beam spot size, a beam intensity of 1.92 nA after the 1 mm hole collimator is required, which is about one-tenth of the value that a cyclotron can provide. This 50 MeV proton microbeam system will enable the study of the low-dose effect of biological sample irradiation and the radiation resistance of space devices with micron-sized precision.

5 Conclusion

In summary, the beam optics design of a microbeam system with micron-sized resolution based on a cyclotron capable of delivering 50 MeV protons was investigated in this study. The beam optical parameters of an Oxford triplet lens system were calculated using WinTRAX and Zgoubi. Because of the small aberration coefficients of the Oxford triplet lens configuration, the final beam spot size was insensitive to changes in the divergence angle and momentum spread. In addition, the energy collimator of a 90-degree bending magnet and slit system enable the filtering of the momentum spread of the ions. The parasitic aberration coefficients and fringe fields of the quadrupole lens were calculated to evaluate the stability of the final beam spot size. To minimize distortion and increase the final beam spot size, the power supply ripple of the triplet lens should be less than 9×10^{-5}, and the final spot size does not change greatly in the presence of the lens fringe field. The scattering of 50 MeV protons in a slit system has also been studied. According to the simulation, the proportion of scattered protons that can enter the quadrupole lens group is acceptable because the energies of most of the scattered protons are much lower than 50 MeV. For radiation protection of the 50 MeV proton microbeam system, the shielding of neutrons, gamma rays and electrons must be considered at the slit location. Therefore, a 50 MeV proton microbeam system based on a cyclotron with a micron-sized beam spot is feasible.

Acknowledgements The authors acknowledge G.W. Grime (University of Surrey) for technical communication and for providing the computer software WinTRAX, and François Méot (Brookhaven National

Laboratory) and D. N. Jamieson (The University of Melbourne) for providing the computer software Zgoubi and PRAM, respectively.

Author contributions All authors contributed to the study conception and design. Material preparation, data collection and analysis were performed by Hong-Jin Mou, Guang-Bo Mao and Guang-Hua Du. The first draft of the manuscript was written by Hong-Jin Mou and all authors commented on previous versions of the manuscript. All authors read and approved the final manuscript.

Data availability The data that support the findings of this study are openly available in Science Data Bank at https://doi.org/10.57760/sciencedb.j00186.00078 and https://cstr.cn/31253.11.sciencedb.j00186.00078

Declarations

Conflict of interest The authors declare that they have no competing interests.

References

1. J.C. Chancellor, G.B. Scott, J.P. Sutton, Space radiation: the number one risk to astronaut health beyond low earth orbit. Life (Basel). **4**, 491–510 (2014). https://doi.org/10.3390/life4030491
2. A. Kronenberg, F.A. Cucinotta, Space radiation protection issues. Health Phys. **103**, 556–567 (2012). https://doi.org/10.1097/HP.0b013e3182690caf
3. G.D. Badhwar, P.M. O'Neill, Long-term modulation of galactic cosmic radiation and its model for space exploration. Adv. Space Res. **14**, 749–757 (1994). https://doi.org/10.1016/0273-1177(94)90537-1
4. F.A. Cucinotta, H. Nikjoo, D.T. Goodhead, The effects of delta rays on the number of particle-track traversals per cell in laboratory and space exposures. Radiat. Res. **150**, 115–119 (1998). https://doi.org/10.2307/3579651
5. L.W. Townsend, F.A. Cucinotta, J.W. Wilson et al., Estimates of HZE particle contributions to SPE radiation exposures on interplanetary missions. Adv. Space Res. **14**, 671–674 (1994). https://doi.org/10.1016/0273-1177(94)90524-X
6. J.A. Cookson, F.D. Pilling, The use of focused ion beams for analysis. Thin Solid Films **19**, 381–385 (1973). https://doi.org/10.1016/0040-6090(73)90074-6
7. J.A. van Kan, A.A. Bettiol, F. Watt, Three-dimensional nanolithography using proton beam writing. Appl. Phys. Lett. **83**, 1629–1631 (2003). https://doi.org/10.1063/1.1604468
8. F. Watt, M.B.H. Breese, A.A. Bettiol et al., Proton beam writing. Mater. Today. **10**, 20–29 (2007). https://doi.org/10.1016/S1369-7021(07)70129-3
9. P. Barberet, H. Seznec, Advances in microbeam technologies and applications to radiation biology. Radiat. Prot. Dosim. **166**, 182–187 (2015). https://doi.org/10.1093/rpd/ncv192
10. K.-D. Greif, H.J. Brede, D. Frankenberg et al., The PTB single ion microbeam for irradiation of living cells. Nucl. Instrum. Methods B **217**, 505–512 (2004). https://doi.org/10.1016/j.nimb.2003.11.082
11. C. Siebenwirth, C. Greubel, S.E. Drexler et al., Determination of the accuracy for targeted irradiations of cellular substructures at SNAKE. Nucl. Instrum. Methods B **348**, 137–142 (2015). https://doi.org/10.1016/j.nimb.2015.01.064
12. G.H. Du, J.L. Guo, R.Q. Wu et al., The first interdisciplinary experiments at the IMP high energy microbeam. Nucl. Instrum. Methods B **348**, 18–22 (2015). https://doi.org/10.1016/j.nimb.2015.01.066
13. C. Greubel, W. Assmann, C. Burgdorf et al., Scanning irradiation device for mice in vivo with pulsed and continuous proton beams. Radiat. Environ. Biophys. **50**, 339–344 (2011). https://doi.org/10.1007/s00411-011-0365-x
14. W. Lijun, W. Shaohu, Y. Zengliang, T.K. Hei, G. Randers-Pehrson, Columbia University microbeam: development of an experimental system for targeting cells individually with counted particles. Nucl. Sci. Tech. **10**, 143–148 (1999)
15. F. Watt, X. Chen, C.B. Chen et al., Whole cell structural imaging at 20 nanometre resolutions using MeV ions. Nucl. Instrum. Methods B **306**, 6–11 (2013). https://doi.org/10.1016/j.nimb.2012.11.047
16. W.-T. Yang, X.-C. Du, Y.-H. Li et al., Single-event-effect propagation investigation on nanoscale system on chip by applying heavy-ion microbeam and event tree analysis. Nucl. Sci. Tech. **32**, 106 (2021). https://doi.org/10.1007/s41365-021-00943-6
17. Y.-Q. Yang, W.-C. Fang, X.-X. Huang et al., Static superconducting gantry-based proton CT combined with X-ray CT as prior image for FLASH proton therapy. Nucl. Sci. Tech. **34**, 11 (2023). https://doi.org/10.1007/s41365-022-01163-2
18. H. Zhang, J.-Z. Li, R. Hou et al., Design and development of an ACCT for the Shanghai advanced proton therapy facility. Nucl. Sci. Tech. **33**, 126 (2022). https://doi.org/10.1007/s41365-022-01106-x
19. X.-S. Sun, Y.-J. Li, J.-Y. Liu et al., Shortening the delivery time of proton therapy by real-time compensation method with raster scanning. Nucl. Sci. Tech. **33**, 73 (2022). https://doi.org/10.1007/s41365-022-01051-9
20. B. Qin, X. Liu, Q.-S. Chen et al., Design and development of the beamline for a proton therapy system. Nucl Sci Tech. **32**, 138 (2021). https://doi.org/10.1007/s41365-021-00975-y
21. C.G. Ren, S.J. Zhou, J.M. Che et al., A microbeam system of high energy ions at Fudan university. Nucl. Sci. Tech. **2**, 13–18 (1991)
22. G. Datzmann, G. Dollinger, G. Hinderer et al., A superconducting multipole lens for focusing high energy ions. Nucl. Instrum. Methods B **158**, 74–80 (1999). https://doi.org/10.1016/S0168-583X(99)00308-0
23. J.S.C. Mckee, G.R. Smith, Y.H. Yeo et al., The manitoba automated high-energy proton microprobe (MA-HEM) and its application to research in the geological and biological sciences. Nucl. Instrum. Methods B **40**, 680–684 (1989). https://doi.org/10.1016/0168-583X(89)91074-4
24. L.N. Sheng, M.T. Song, X.Q. Zhang et al., Design of the IMP microbeam irradiation system for 100 MeV/u heavy ions. Chin. Phys. C **33**, 315 (2009). https://doi.org/10.1088/1674-1137/33/4/016
25. A. Ponomarov, G.H. Du, J.L. Guo et al., Beam optics of upgraded high energy heavy ion microbeam in Lanzhou. Nucl. Instrum. Methods B **461**, 10–15 (2019). https://doi.org/10.1016/j.nimb.2019.09.002
26. T. Vallentin, M. Moser, S. Eschbaumer et al., A microbeam slit system for high beam currents. Nucl. Instrum. Methods B **348**, 43–47 (2015). https://doi.org/10.1016/j.nimb.2014.12.015
27. M. Oikawa, T. Kamiya, M. Fukuda et al., Design of a focusing high-energy heavy ion microbeam system at the JAERI AVF cyclotron. Nucl. Instrum. Methods B **210**, 54–58 (2003). https://doi.org/10.1016/S0168-583X(03)01007-3
28. F. Watt, G.W. Grime, G.D. Blower et al., The Oxford 1 μm proton microprobe. Nucl. Instrum. Methods **197**, 65–77 (1982). https://doi.org/10.1016/0167-5087(82)90119-3
29. G.W. Grime, WinTRAX: A raytracing software package for the design of multipole focusing systems. Nucl. Instrum. Methods B **306**, 76–80 (2013). https://doi.org/10.1016/j.nimb.2012.11.038

30. F. Méot, The ray-tracing code Zgoubi. Nucl. Instrum. Methods A **427**, 353–356 (1999). https://doi.org/10.1016/S0168-9002(98)01508-3
31. F. Méot, The ray-tracing code Zgoubi–Status. Nucl. Instrum. Methods A **767**, 112–125 (2014). https://doi.org/10.1016/j.nima.2014.07.022
32. M.B.H. Breese, D.N. Jamieson, P.J.C. King, Material analysis using a nuclear microprobe. J. Microsc-Oxford. **189**, 99–100 (1996). https://doi.org/10.1046/j.1365-2818.1998.0270c.x
33. C.G. Ryan, PIXE and the nuclear microprobe: tools for quantitative imaging of complex natural materials. Nucl. Instrum. Methods B **269**, 2151–2162 (2011). https://doi.org/10.1016/j.nimb.2011.02.046
34. V. Brazhnik, A. Dymnikov, R. Hellborg et al., The effect of lens arrangement in a triplet and in a Russian quadruplet on the demagnification and beam current in a microprobe. Nucl. Instrum. Methods B **77**, 29–34 (1993). https://doi.org/10.1016/0168-583X(93)95518-A
35. Y.X. Dou, D.N. Jamieson, J.L. Liu et al., GEANT4 models for the secondary radiation flux in the collimation system of a 300MeV proton microbeam. Phys. Med. **32**, 1841–1845 (2016). https://doi.org/10.1016/j.ejmp.2016.10.008
36. G.W. Grime, F. Watt, G.D. Blower et al., Real and parasitic aberrations of quadrupole probe-forming systems. Nucl. Instrum. Methods. **197**, 97–109 (1982). https://doi.org/10.1016/0167-5087(82)90123-5
37. S. Incerti, P. Barberet, R. Villeneuve et al., Simulation of cellular irradiation with the CENBG microbeam line using GEANT4. IEEE Trans. Nucl. Sci. **51**, 1395–1401 (2004). https://doi.org/10.1109/TNS.2004.832224
38. L.N. Sheng, M.T. Song, X.Q. Zhang et al., High energy heavy ion microbeam irradiation facility at IMP. Nucl. Instrum. Methods B **269**, 2189–2192 (2011). https://doi.org/10.1016/j.nimb.2011.02.075
39. G.H. Du, Techniques and multi-disciplinary applications of ion microbeam. Nucl. Phys. Rev. **29**, 371 (2012). https://doi.org/10.11804/NuclPhysRev.29.04.371
40. J.F. Ziegler, M.D. Ziegler, J.P. Biersack, SRIM—the stopping and range of ions in matter (2010). Nucl. Instrum. Methods B **268**, 1818–1823 (2010). https://doi.org/10.1016/j.nimb.2010.02.091
41. S. Agostinelli, J. Allison, K. Amako et al., Geant4—a simulation toolkit. Nucl. Instrum. Methods A **506**, 250–303 (2003). https://doi.org/10.1016/S0168-9002(03)01368-8